RSC Advances

PAPER

View Article Online
View Journal | View Issue

Cite this: *RSC Adv.*, 2025, **15**, 31508

Construction of a 1D/0D/2D $BiFeO_3$/Ag/g-C_3N_4 Z-scheme heterojunction for enhanced visible light photocatalysis of methylene blue

Donghai Li, Yunrui Xu, Shilin Zhang and Linping Wang *

To improve the utilization of solar energy and the efficiency of photocatalytic organic pollutant degradation, novel Z-scheme heterojunctions with high visible light catalytic performances have been widely developed. Herein, a novel Z-scheme $BiFeO_3$/Ag/g-C_3N_4 heterojunction with a hierarchical 1D/0D/2D structure and visible light absorption was constructed by matching the suitable band structure between 1D $BiFeO_3$ and 2D g-C_3N_4 and employing the localized surface plasmon resonance (LSPR) effect of 0D Ag nanoparticles. $BiFeO_3$ nanofibers were synthesized *via* the electrospinning technique, providing short electron transport paths and visible light absorption range for g-C_3N_4. Plasmonic Ag nanoparticles were photodeposited on the surface of $BiFeO_3$ to enhance the separation efficiency of the photogenerated electron–hole pairs between the bulk interfaces. UV-vis DRS, PL, photocurrent and EIS spectra confirmed the important roles of Ag and $BiFeO_3$ in improving the photocatalytic activity of the Z-scheme heterojunction. The working principle of the $BiFeO_3$/Ag/g-C_3N_4 Z-scheme heterojunction was proposed, indicating that $^{\bullet}O_2^-$ and $^{\bullet}OH$ are the main active species for the photocatalytic degradation of methylene blue (MB). The prepared $BiFeO_3$/Ag/g-C_3N_4 heterojunction exhibited the highest photocatalytic activity, where its rate constant was 5.84 times higher than that of the pristine $BiFeO_3$ and 3.26 times higher than that of the pristine g-C_3N_4. This study offers a new means for the design of novel high-performance photocatalysts, which can be a promising candidate in industrial applications.

Received 6th July 2025
Accepted 19th August 2025

DOI: 10.1039/d5ra04825g

rsc.li/rsc-advances

1. Introduction

Nowadays, solar-based photocatalytic technology is a promising solution to the global energy crisis and environmental remediation, including photocatalytic hydrogen production, photocatalytic reduction of CO_2 and photocatalytic degradation of organic pollutants.[1] Methylene blue (MB), a sulphur-containing cationic dye, is regarded as a common pollutant in wastewater discharged from textile industries.[2–5] MB poses a carcinogenic risk to humans and many aquatic organisms and affects the balance of the entire aquatic ecosystem.[6] Photocatalytic degradation of MB is considered a high-efficiency, low-cost and environmentally friendly water treatment technology, which needs high-performance photocatalysts for the decomposition of MB into CO_2, H_2O and some harmless organic molecules.[7] However, single photocatalytic materials, such as TiO_2, suffer from the drawbacks of low utilization of the visible light, easy recombination of the photogenerated electron–hole pairs, and low photocatalytic activity.[8,9] As a typical 2D conjugated polymer photocatalyst, g-C_3N_4 possesses the advantages of low cost, non-toxicity, and high specific surface area.[10,11] However, g-C_3N_4 can absorb sunlight only at wavelengths below 460 nm and has a low valence band level ($E_{VB} = 1.50$ eV), which is lower than the oxidation potential for the generation of hydroxyl radicals ($^{\bullet}OH$), and thus, its efficiency for the photocatalytic degradation of pollutants is significantly weakened.[12]

To enhance the photocatalytic activity of photocatalysts, numerous strategies have been explored, such as defect engineering, ion doping, and heterojunction construction.[13–15] Among the numerous approaches, heterojunction construction is regarded as a promising strategy due to its merits in promoting photogenerated carrier separation and enhancing the light absorption and stability.[16] Generally, the interface structures of heterojunctions are composed of two or more different semiconductor materials, which can be divided into type I, type II, and Z-schemes. Compared with type I and type II heterojunctions, Z-scheme heterojunctions enable efficient electron–hole separation with great retention of redox capability. Zheng *et al.* prepared a WO_3/g-C_3N_4 Z-scheme photocatalyst by calcination and hydrothermal treatment to achieve high redox capacity, efficient charge separation and large reaction surface area for the photocatalytic degradation of dodecylmorpholine (DMP), and its degradation efficiency was 73% in 60 min.[17] However, the electron transfer rate between heterojunction interfaces greatly affects the efficiency for the photocatalytic degradation of pollutants. In this case, the incorporation of metal nanoparticles exhibiting localized

College of Chemical Engineering, Qinghai University, Xining-810016, China. E-mail: wanglp@qhu.edu.cn

surface plasmon resonance (LSPR) within Z-scheme heterojunctions can accelerate the electron transfer rate across the interface and broaden the absorption spectrum to visible light with enhanced the solar energy utilisation. The Schottky junction at the interface between the metal and the semiconductor inhibits the compounding of photogenerated carriers.

As a typical multiferroic perovskite material, $BiFeO_3$ exhibits excellent photovoltaic, thermal, specific ferroelectric and magnetic properties. Especially in the field of photocatalysis, its polarization effect leads to band bending, resulting in the effective separation of excitons.[18,19] In this study, $BiFeO_3$ nanofibres with a suitable band gap ($E_{CB} = 0.51$ eV, $E_{VB} = 2.61$ eV, and $E_g = 2.10$ eV) are matched with g-C_3N_4 ($E_{CB} = -1.22$ eV, $E_{VB} = 1.50$ eV, and $E_g = 2.72$ eV) to form an ideal Z scheme heterojunction.[20,21] The $BiFeO_3$ nanofibres with a large aspect ratio can largely shorten the photogenerated electron transfer pathways.[22] The Ag nanoparticles acted as a direct electron bridge between $BiFeO_3$ and g-C_3N_4 to construct an efficient Z-scheme heterojunction, which reduced the electron transfer resistance between the interfaces.[23] The LSPR effect of the Ag nanoparticles further broadened the light absorption range and lowered the Schottky barrier to enhance the solar energy utilization. We achieved the degradation of MB using the 1D/0D/2D $BiFeO_3$/Ag/g-C_3N_4 Z-scheme heterojunction and proposed its rational mechanism *via* free radical trapping experiments. This study provides new insights into the development of high-performance Z-scheme photocatalysts for the efficient photocatalytic degradation of pollutants in wastewater.

2. Experimental

2.1. Materials

Bismuth nitrate pentahydrate ($Bi(NO_3)_3 \cdot 5H_2O$, 99.9%), melamine ($C_3H_6N_6$, 99%), iron(III) nitrate nonahydrate ($Fe(NO_3)_3 \cdot 9H_2O$, 99.9%) and polyvinylpyrrolidone (PVP) with an average molecular weight of 1 200 000 were purchased from Shanghai Aladdin Reagent Co., Ltd. Silver nitrate ($AgNO_3$, 99.8%) was purchased from Oubokai Chemical Co., Ltd. *N*,*N*-Dimethylformamide (DMF, 99.5%) and acetone (AC, C_3H_6O, 99.5%) were purchased from Shanghai Guoyao Group Chemical Reagent Co., Ltd. Anhydrous ethanol (C_2H_5OH, 99.7%) and methanol (CH_3OH, 99.5%) were purchased from Chengdu Chron Chemical Co., Ltd. Methylene blue ($C_{16}H_{18}N_3ClS$, 98.5%) was purchased from Shanghai Zhanyun Chemical Co., Ltd.

2.2. Synthesis of g-C_3N_4

g-C_3N_4 was prepared by pyrolyzing melamine.[24] In detail, 10 g of melamine powder was initially placed in a lidded ceramic crucible and subjected to heating in a muffle furnace. The furnace was heated at a rate of 5 °C min^{-1} until the temperature reached 550 °C and was maintained at this temperature for 2 h. At the end of the calcination process, the material was cooled naturally to room temperature and ground with a mortar and pestle to obtain the final g-C_3N_4 powder.

2.3. Synthesis of $BiFeO_3$

$BiFeO_3$ nanofibres were prepared by the electrospinning method. 1.00 g $Bi(NO_3)_3 \cdot 5H_2O$ and 0.75 g $Fe(NO_3)_3 \cdot 9H_2O$ were dissolved in 2.50 mL ultrapure water, and then 1.50 mL glacial acetic acid was added and stirred for 2 h. In parallel, 0.93 g PVP was dissolved in 5.63 mL mixed solution of AC and DMF (AC/DMF = 1 : 2). These two solutions were mixed and stirred for 4 h to obtain a golden-yellow precursor solution for electrostatic spinning. An applied voltage of 16.50 kV and an advancement speed of 0.05 mm min^{-1} were used to obtain the $BiFeO_3$ nanofibre precursor. The $BiFeO_3$ nanofibre precursor was placed in a muffle furnace and heated to 550 °C for 2 h at a ramp rate of 1 °C min^{-1}. The calcined samples were cooled to room temperature in an air environment and placed in an onyx mortar for grinding to obtain pure $BiFeO_3$ nanofibres.

2.4. Synthesis of $BiFeO_3/Ag_x$

The $BiFeO_3/Ag_x$ compound was synthesised *via* the photodeposition of Ag nanoparticles on $BiFeO_3$ nanofibres by using CH_3OH as a reducing agent. 0.1 g $BiFeO_3$ nanofibres and a certain amount of $AgNO_3$ were added to a mixed solution of 10 mL CH_3OH and 40 mL H_2O, and sonicated for 10 min. The mixed solution was irradiated by a xenon lamp for 2 h. After irradiation, the mixed solution was centrifuged at 12 000 rpm for 10 min, washed twice with ethanol, and dried under vacuum at 60 °C for 12 h to obtain the $BiFeO_3/Ag_x$ samples, where x denotes the mass fraction of Ag.

2.5. Synthesis of $(BiFeO_3/Ag_x)/(g\text{-}C_3N_4)_y$

0.1 g of synthesised g-C_3N_4 was added to 50 mL of ultrapure water and sonicated for 0.5 h to form a homogeneous solution. A certain amount of $BiFeO_3/Ag_x$ was dissolved in the solution of g-C_3N_4 and ultrasonicated for 2 h. The mixed solution was subsequently centrifuged at 12 000 rpm, and the resulting precipitate was dried under vacuum at 60 °C for 24 h to obtain the $(BiFeO_3/Ag_x)/(g\text{-}C_3N_4)_y$ composites, where the ratio of y is defined as the mass fraction of g-C_3N_4, as shown in Fig. 1.

2.6. Characterization

The morphologies of the samples were characterized using a scanning electron microscope (SEM, JSM-7900F, JEOL). The elemental composition of the samples was characterized using an energy-dispersive X-ray spectrometer (EDX, JSM-7900F, JEOL). The specific surface area of the photocatalyst was determined using a fully automatic specific surface area and porosity analyzer (BET, ASAP 2460, Micromeritics). The phase identification of the samples was performed on a powder X-ray diffractometer (XRD, Ultima IV, Rigaku). Elemental states and surface chemistry were examined by X-ray photoelectron spectroscopy (XPS, Nexsa G2, Thermo Fisher). The absorbance of the pollutants was determined by ultraviolet-visible spectroscopy (UV-vis, UV-2550, Shimadzu). The functional groups of the materials were tested using a Fourier transform infrared spectrometer (FTIR, VERTEX70V, Bruker). The photogenerated electron–hole pair recombination rates were analysed using

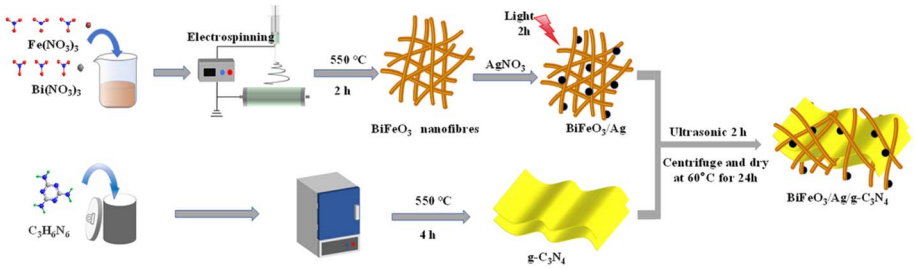

Fig. 1 Schematic of the preparation of $BiFeO_3$/Ag/g-C_3N_4.

a photoluminescence spectrometer (PL, Cary Eclipse, Agilent), operating at room temperature with an excitation wavelength of 300 nm. The light absorption performances of the samples were tested using a solid-state ultraviolet-visible diffuse reflectance spectrometer (DRS, Cary 5000, Agilent). The intermediate products of the photocatalytic degradation of MB were determined by liquid chromatography-mass spectrometry (LC-MS, Integrion + TSQ Fortis Plus, Thermo Scientific).

2.7. Electrochemical measurements

Photoelectrochemical properties were measured by means of a conventional three-electrode system. Sample-modified indium tin oxide-coated glass was used as the working electrode, a carbon rod as the counter electrode, and a saturated calomel electrode as the reference electrode. In the photocurrent tests, a 0.1 mol L^{-1} ascorbic acid (AA) solution was used as the electrolyte and a 300 W xenon lamp was used as the light source, which was switched on and off at 20 s intervals during the test period of 0–160 s. In the Nyquist plot measurements, a 2.0 mM 1 : 1 $K_3[Fe(CN)_6]/K_4[Fe(CN)_6]$ and 0.1 mol L^{-1} Na_2SO_4 solution was used as the electrolyte with an applied bias voltage of 0.2 V. In the Mott–Schottky tests, a 0.5 mol L^{-1} Na_2SO_4 solution was used as the electrolyte.

2.8. Photocatalytic activity evaluation

The catalytic performance of the prepared samples was evaluated using MB solution under simulated sunlight (xenon lamp = 300 W). 10 mg catalyst was added to 50 mL of MB solution (c = 10 mg L^{-1}) at room temperature and magnetically stirred in the dark for 30 min to ensure adsorption and desorption equilibrium. Under light illumination, 2 mL of the suspension was collected and filtered through a 0.45 μm mixed cellulose ester (MCE) membrane. The photocatalytic activity of the catalyst was analyzed by measuring its absorbance at 664 nm on a UV-vis spectrophotometer.

3. Results

3.1. Morphology and structure analysis

3.1.1. XRD analysis. The XRD analysis confirmed the successful preparation of g-C_3N_4, $BiFeO_3$, and ($BiFeO_3$/$Ag_{0.05}$)/(g-C_3N_4)$_{0.3}$, as shown in Fig. 2a. The main diffraction peak located at the 2θ value of 27.5° is attributed to the (002) crystal plane of g-C_3N_4 (JCPDS no. 50-1512).[25] The main diffraction peaks for the prepared $BiFeO_3$ at 2θ = 22.5°, 32.1°, 32.3°, 39.8°, 45.8°, and 52.3° correspond to the (012), (104), (110), (202), (024), and (116) crystal planes of $BiFeO_3$, respectively (JCPDS no. 86-1518).[26] Comparatively, ($BiFeO_3$/$Ag_{0.05}$)/(g-C_3N_4)$_{0.3}$ exhibits the main characteristic peaks of $BiFeO_3$, g-C_3N_4, and Ag for the (111), (200), and (220) crystal planes at 2θ = 37.6°, 44.0° and 63.8°, respectively (JCPDS no. 65-2871).[27] We performed Rietveld refinement on ($BiFeO_3$/$Ag_{0.05}$)/(g-C_3N_4)$_{0.3}$. As shown in Fig. 2b, peaks corresponding to the g-C_3N_4 phase, $BiFeO_3$ phase, and Ag^0 phase can clearly be observed. By simulating g-C_3N_4 (a = 6.4505 Å, b = 6.4505 Å, c = 2.4231 Å and V = 87.3171 $Å^3$),[28] $BiFeO_3$ (a = 5.5881 Å, b = 5.5881 Å, c = 13.9072 Å and V = 376.0994 $Å^3$),[29] and Ag (a = 4.0842 Å, b = 4.0842 Å, c = 4.0842 Å

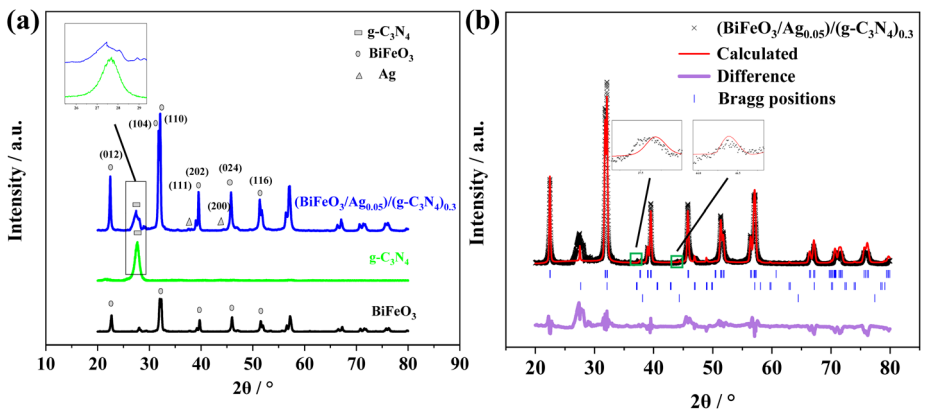

Fig. 2 (a) XRD patterns of g-C_3N_4, $BiFeO_3$, and ($BiFeO_3$/$Ag_{0.05}$)/(g-C_3N_4)$_{0.3}$. (b) Rietveld refinement XRD patterns of ($BiFeO_3$/$Ag_{0.05}$)/(g-C_3N_4)$_{0.3}$.

Table 1 Microstructural parameters obtained from the Rietveld analysis of $(BiFeO_3/Ag_{0.05})/(g\text{-}C_3N_4)_{0.3}$

Sample	Phase	Space group	a (Å)	b (Å)	c (Å)	V (Å^3)	R_{WP} (%)	R_P (%)	Volume (%)
	JCPDS no. 50-1512	$P6_3/m$	6.4505	6.4505	2.4231	87.3171	—	—	—
	JCPDS no. 86-1518	$R3c$	5.5881	5.5881	13.9072	376.0994	—	—	—
	JCPDS no. 65-2871	$Fm\bar{3}m$	4.0842	4.0842	4.0842	68.1923	—	—	—
$(BiFeO_3/Ag_{0.05})/(g\text{-}C_3N_4)_{0.3}$	$g\text{-}C_3N_4$	$P6_3cm$	6.4456	6.4456	2.4206	87.1032	1.20	0.82	33.1
	$BiFeO_3$	$R3c$	5.5786	5.5786	13.8601	373.5562			65.1
	Ag	$Fm\bar{3}m$	4.0683	4.0683	4.0683	68.1923			1.8

and $V = 68.1923$ Å^3),[30] we obtained the lattice parameters and phase composition of the material. As shown in Table 1, the lattice parameters of $g\text{-}C_3N_4$ ($a = 6.4456$ Å, $b = 6.4456$ Å, $c = 2.4206$ Å and $V = 87.1032$ Å^3), $BiFeO_3$ ($a = 5.5786$ Å, $b = 5.5786$ Å, $c = 13.8601$ Å and $V = 373.5562$ Å^3), and Ag ($a = 4.0683$ Å, $b = 4.0683$ Å, $c = 4.0683$ Å and $V = 68.1923$ Å^3) are almost identical to their standard card values, indicating that the synthesized material has high crystallinity and purity.

3.1.2. SEM analysis. The micromorphology of the catalysts was investigated by SEM. As shown in Fig. 3a, $BiFeO_3$ exhibits a fibrous structure that is continuous and uniformly dispersed with a diameter of around 100 nm. The Ag nanoparticles are decorated on the $BiFeO_3$ nanofibers with a particle size in the range of 10 to 20 nm (Fig. 3b). Non-uniform broken $BiFeO_3$ nano-fibers are formed due to the photodeposition of Ag nanoparticles on $BiFeO_3$. After the combination of $BiFeO_3$/Ag with $g\text{-}C_3N_4$, flake-like $g\text{-}C_3N_4$ appeared in the nanofibers (Fig. 3c). The 1D/0D/2D $BiFeO_3$/Ag/$g\text{-}C_3N_4$ multidimensional structure increases the specific surface area of the single materials, which was further confirmed by the N_2 adsorption–desorption isotherm tests. The N_2 adsorption–desorption isotherm curves are displayed in Fig. S1, and the specific surface

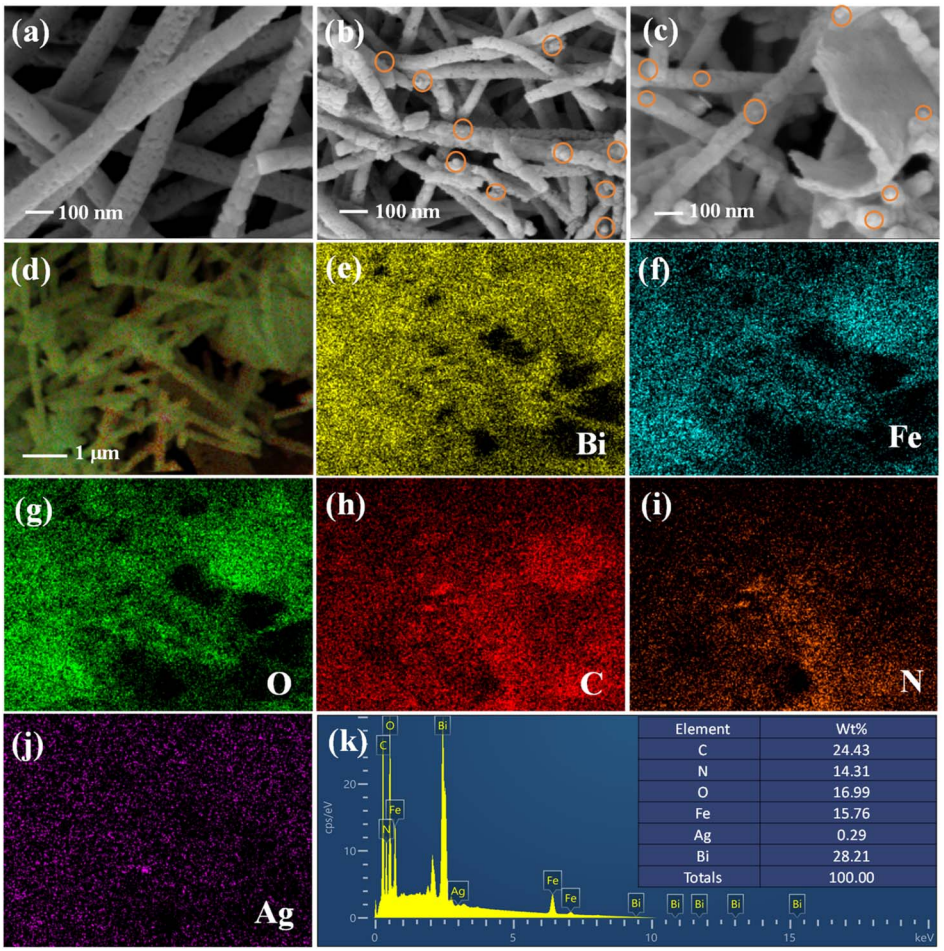

Fig. 3 SEM images of (a) $BiFeO_3$, (b) $BiFeO_3/Ag_{0.05}$, and (c) $(BiFeO_3/Ag_{0.05})/(g\text{-}C_3N_4)_{0.3}$ and (d–k) EDX element mapping of $(BiFeO_3/Ag_{0.05})/(g\text{-}C_3N_4)_{0.3}$.

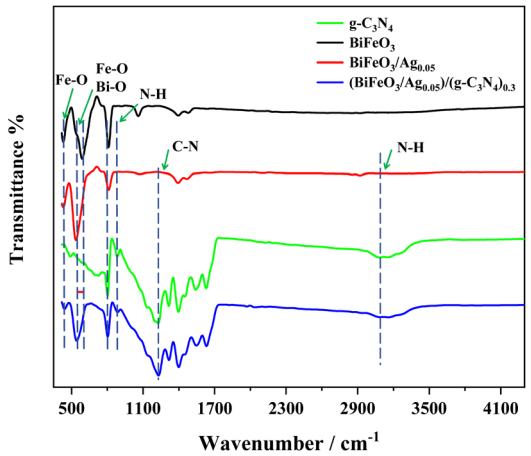

Fig. 4 FT-IR spectra of g-C_3N_4, $BiFeO_3$, $BiFeO_3/Ag_{0.05}$, and $(BiFeO_3/Ag_{0.05})/(g\text{-}C_3N_4)_{0.3}$.

area and pore volume values are displayed in Table S1. The surface area of $(BiFeO_3/Ag_{0.05})/(g\text{-}C_3N_4)_{0.3}$ is obviously higher than that of g-C_3N_4 and $BiFeO_3$/Ag, facilitating the greater exposure of reactive sites to further improve the efficient ion transport and photocatalytic degradation ability. The EDX analysis confirms the presence of Bi, Fe, O, C, N and Ag elements in the $(BiFeO_3/Ag_{0.05})/(g\text{-}C_3N_4)_{0.3}$ composite, indicating the successful preparation of the $BiFeO_3$/Ag/g-C_3N_4 heterojunction (Fig. 3d–k). The presence of Bi, Fe, O, C, N and Ag elements evenly distributed with mass ratios of 28.21%, 15.76%, 16.99%, 24.43%, 14.31%, and 0.29%, respectively, indicates the successful incorporation of a certain amount of Ag in the composite.

3.1.3. FTIR analysis. FTIR spectroscopy was employed to determine the surface functional groups in g-C_3N_4, $BiFeO_3$, $BiFeO_3/Ag_{0.05}$, and $(BiFeO_3/Ag_{0.05})/(g\text{-}C_3N_4)_{0.3}$, as shown in Fig. 4. In the spectrum of g-C_3N_4, the absorption peaks at 805 cm^{-1}, 887 cm^{-1}, 1230 cm^{-1}, and 3140 cm^{-1} are attributed to the triazine breathing mode, the deformation mode of N–H, and the stretching vibration of the C–N and N–H bond, respectively.[31–34] The peaks at 440 cm^{-1} and 544 cm^{-1} are attributed to the bending vibrations of Fe–O in the octahedral FeO_6 groups, and the stretching vibrations of Fe–O and Bi–O.[35] After Ag nanoparticles were deposited on the surface of $BiFeO_3$, a blue-shift in the absorption peak was observed from 544 cm^{-1} to 538 cm^{-1}.[36] The spectrum of $(BiFeO_3/Ag_{0.05})/(g\text{-}C_3N_4)_{0.3}$ contains peaks related to g-C_3N_4, and two characteristic $BiFeO_3/Ag_{0.05}$ peaks at 440 and 538 cm^{-1}, confirming the successful fabrication of the heterojunction structure.

3.1.4. XPS analysis. To further pursue the chemical state and composition of the elements in the as-prepared $(BiFeO_3/Ag_{0.05})/(g\text{-}C_3N_4)_{0.3}$, its XPS spectrum was recorded, as shown in Fig. 5. Fig. 5a shows the main elements of Fe, Bi, O, N, C and Ag in $(BiFeO_3/Ag_{0.05})/(g\text{-}C_3N_4)_{0.3}$. Fig. 5b–g represent the high-resolution XPS spectra of Bi 4f, Fe 2p, O 1s, C 1s, N 1s and Ag

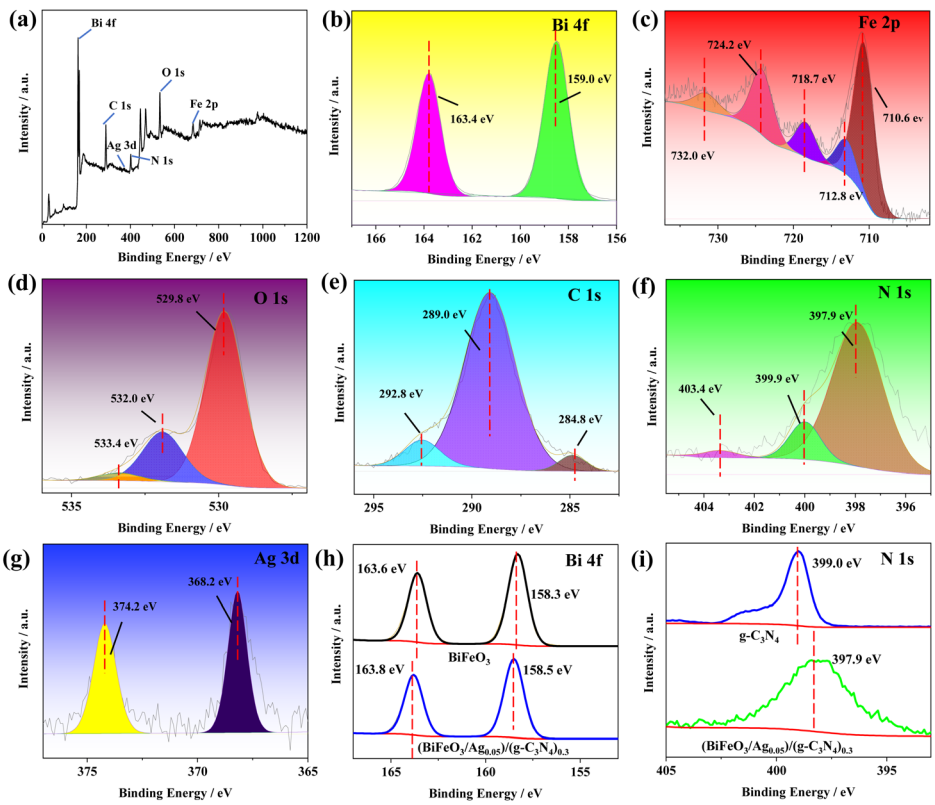

Fig. 5 (a) XPS spectrum of $(BiFeO_3/Ag_{0.05})/(g\text{-}C_3N_4)_{0.3}$. (b–g) Narrow-scan XPS of $(BiFeO_3/Ag_{0.05})/(g\text{-}C_3N_4)_{0.3}$ in the regions of Bi 4f, Fe 2p, O 1s, C 1s, N 1s, and Ag 3d core levels, respectively. (h) Comparison of the XPS spectra of $BiFeO_3$ and $(BiFeO_3/Ag_{0.05})/(g\text{-}C_3N_4)_{0.3}$ for Bi 4f. (i) Comparison of the XPS spectra of g-C_3N_4 and $(BiFeO_3/Ag_{0.05})/(g\text{-}C_3N_4)_{0.3}$ for N 1s.

3d, respectively. The Bi 4f spectrum exhibits doublet peaks at 163.4 eV and 159.0 eV, corresponding to Bi $4f_{5/2}$ and Bi $4f_{7/2}$ of Bi^{3+}, respectively.[37] The Fe 2p spectrum of $(BiFeO_3/Ag_{0.05})/(g\text{-}C_3N_4)_{0.3}$ exhibits three peaks at 710.7 eV, 712.8 eV, and 724.2 eV, which correspond to Fe^{2+} $2p_{3/2}$, Fe^{3+} $2p_{3/2}$, and Fe^{3+} $2p_{1/2}$, respectively. The other peaks centered at 732.0 eV and 718.7 eV are designated as Fe^{3+} satellite peaks.[38,39] The XPS O 1s spectrum displays three peaks at 529.8 eV, 532.0 eV and 533.4 eV, corresponding to the surface lattice oxygen, surface hydroxyl groups and surface adsorbed oxygen.[40] In the C 1s XPS spectrum, the peak at 289.0 eV is typically associated with the N–C=N in the triazine units, the peak at 284.8 eV is attributed to C–O species on the surface of g-C_3N_4, and the peak at 292.8 eV can be assigned to π electronic excitation.[41,42] In the XPS N 1s spectrum, the peak at 397.9 eV is typically attributed to C–N=C, and the peak at 399.9 eV corresponds to N–H.[42] Another peak centered at 403.4 eV is related to pi-excitations on heterocycles.[43] In the Ag 3d XPS spectrum, the peaks at 374.2 eV and 368.2 eV are attributed to Ag $3d_{5/2}$ and Ag $3d_{3/2}$, respectively. The difference between these two peaks is 6 eV, indicating that silver atoms are in a metallic state.[44] To further confirm the electron transfer in the heterojunction, the peak positions of Bi 4f in $BiFeO_3$, and N 1s of g-C_3N_4 were examined by XPS. As shown in Fig. 5h and i, compared with $BiFeO_3$ and g-C_3N_4, the position of Bi 4f in $(BiFeO_3/Ag_{0.05})/(g\text{-}C_3N_4)_{0.3}$ shifted positively by approximately 0.2 eV, while the position of N 1s shifted negatively by approximately 1.1 eV. Similarly, as shown in Fig. 5g, the Ag 3d peak in $(BiFeO_3/Ag_{0.05})/(g\text{-}C_3N_4)_{0.3}$ exhibits a positive shift of approximately 0.2 eV relative to the reported values for Ag^0 (368.0 and 374.0 eV).[45] The peak shifting in $(BiFeO_3/Ag_{0.05})/(g\text{-}C_3N_4)_{0.3}$ demonstrates that electrons could migrate from $BiFeO_3$ to Ag, and then to g-C_3N_4, resulting a fixed Z-scheme heterojunction photocatalytic system at the double interfaces of $BiFeO_3$/Ag and g-C_3N_4/Ag.[46]

3.1.5. UV-vis DRS and PL analysis. The UV-vis absorbance of g-C_3N_4, $BiFeO_3$, $BiFeO_3/Ag_{0.05}$ and $(BiFeO_3/Ag_{0.05})/(g\text{-}C_3N_4)_{0.3}$ was tested using UV-visible diffuse reflectance spectroscopy. As shown in Fig. 6a, g-C_3N_4 has narrow visible light absorption ability, and the absorption edge of g-C_3N_4 is located at 458 nm. The pure-phase $BiFeO_3$ exhibits strong visible light absorption properties in the range of 400–550 nm, and its absorption boundary is located at 619 nm. After loading Ag nanoparticles, the absorption edge of $BiFeO_3/Ag_{0.05}$ is markedly red-shifted to 660 nm. Due to the LSPR effect of the Ag nanoparticles, 'hot' electrons were injected into the $BiFeO_3$ interface, further broadening the light absorption range and lowering the Schottky barrier.[47] The LSPR effect is largely dependent on the size and shape of the Ag nanoparticles, and the LSPR peaks could be tuned to ~450 nm based on the size of Ag nanoparticles in the range of 10–20 nm.[48,49] The $(BiFeO_3/Ag_{0.05})/(g\text{-}C_3N_4)_{0.3}$ heterojunction has an excellent visible light absorption performance with an absorption edge at 594 nm.

PL spectra were used to evaluate the separation rate of photogenerated electron–hole pairs. As shown in Fig. 6b, the PL emission intensity of $BiFeO_3$/Ag is markedly reduced than that of pristine $BiFeO_3$. This indicates that the Ag nanoparticles deposited on the surface of $BiFeO_3$ formed a Schottky junction, which can suppress the recombination of electron–hole pairs at the interface of $BiFeO_3$/Ag. In addition, $BiFeO_3/Ag_{0.05}$ exhibits the lowest intensity, and the intensity of its PL emission peak decreases with an increase in the concentration of Ag nanoparticles. Given that excessive Ag nanoparticles may accumulate, resulting in the formation of composite centers, the separation rate of photogenerated electron–hole pairs decreases.[47] The PL intensity of $(BiFeO_3/Ag_{0.05})/(g\text{-}C_3N_4)_{0.3}$ was significantly reduced compared with that of pure $BiFeO_3$ and g-C_3N_4, indicating that the separation efficiency of the photogenerated electron–hole pairs was higher than that of pure $BiFeO_3$ and g-C_3N_4.

3.1.6. Photocurrent and EIS analysis. Transient photocurrent measurements were performed to investigate the photogenerated carrier separation and interfacial charge transfer efficiency of the samples. As shown in Fig. 7a, the photocurrent intensity of g-C_3N_4 is 0.61 μA, while that of $BiFeO_3$ is 0.65 μA. With the addition of Ag nanoparticles, the photocurrent intensity of $BiFeO_3/Ag_{0.05}$ significantly increased to 1.65 μA, which is attributed to the good conductive ability of the Ag nanoparticles. The photocurrent intensity of $(BiFeO_3/Ag_{0.05})/(g\text{-}C_3N_4)_{0.5}$ is 4.62 μA, which is about 7.57-fold higher than that of g-C_3N_4 and 7.10-fold higher than that of $BiFeO_3$. The

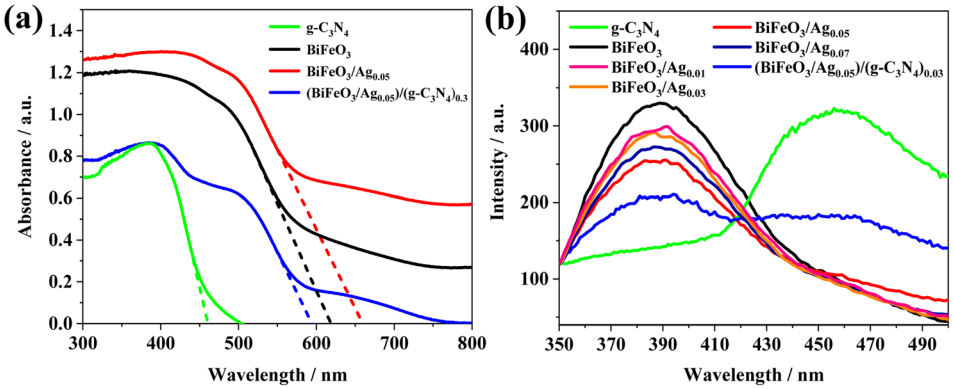

Fig. 6 (a) UV-vis DRS spectra of the as-prepared g-C_3N_4, $BiFeO_3$, $BiFeO_3/Ag_{0.05}$ and $(BiFeO_3/Ag_{0.05})/(g\text{-}C_3N_4)_{0.3}$. (b) PL spectra of g-$C_3N_4$, $BiFeO_3$, $BiFeO_3/Ag_{(0.01-0.07)}$, and $(BiFeO_3/Ag_{0.05})/(g\text{-}C_3N_4)_{0.3}$ (300 nm excitation).

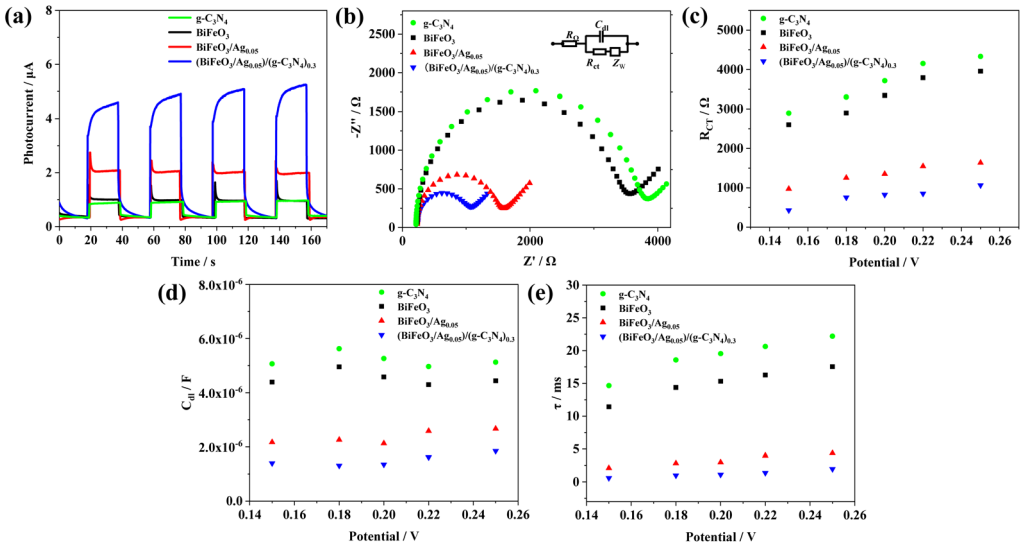

Fig. 7 (a) Photocurrent spectra of g-C_3N_4, $BiFeO_3$, $BiFeO_3/Ag_{0.05}$, and $(BiFeO_3/Ag_{0.05})/(g\text{-}C_3N_4)_{0.3}$. (b) EIS spectra of g-$C_3N_4$, $BiFeO_3$, $BiFeO_3/Ag_{0.05}$ and $(BiFeO_3/Ag_{0.05})/(g\text{-}C_3N_4)_{0.3}$, inset: equivalent circuit (photocurrent responses measured at a bias voltage of 0.0 V (*vs.* SCE) in 0.1 M ascorbic acid and EIS responses measured in 0.1 M Na_2SO_4 containing 2.0 mM 1 : 1 $K_3[Fe(CN)_6]/K_4[Fe(CN)_6]$ after biasing at 0.2 V (*vs.* SCE) for 200 s). Impedance fitting results of (c) R_{ct} and (d) C_{dl} data *versus* the applied potential. (e) Electron lifetimes of the photocatalysts *versus* applied potential.

heterojunction structure of $(BiFeO_3/Ag_{0.05})/(g\text{-}C_3N_4)_{0.3}$ provides a more efficient transport path for photogenerated electrons by the synergistic effect of LSPR Ag, $BiFeO_3$ and g-C_3N_4.

Electrochemical impedance spectroscopy (EIS) of the g-C_3N_4, $BiFeO_3$, $BiFeO_3/Ag_{0.05}$, and $(BiFeO_3/Ag_{0.05})/(g\text{-}C_3N_4)_{0.3}$ modified ITO electrodes was also carried out to evaluate the kinetics of interfacial charge transmission and fitted to the circuit equivalent, the Randles and Ershler model (inset of Fig. 7b).[50] As shown in Fig. 7b, g-C_3N_4 exhibits the largest semicircle with the charge transfer resistance (R_{ct}) value of about 3694 Ω, indicating that g-C_3N_4 possesses poor electron conductive ability. Compared to $BiFeO_3$ (3113 Ω), $BiFeO_3/Ag_{0.05}$ has a significantly lower electrochemical impedance with an R_{ct} value of 1350 Ω for the rapid transfer of carriers by LSPR Ag and formed Schottky junctions. The small amount of Ag loading can significantly lower the charge transfer resistance and exhibit better photogenerated carrier mobility. The $(BiFeO_3/Ag_{0.05})/(g\text{-}C_3N_4)_{0.3}$ heterojunction exhibits a significantly reduced arc radius than that of the other materials with an R_{ct} value of 825 Ω. The lower charge transfer resistance of the $(BiFeO_3/Ag_{0.05})/(g\text{-}C_3N_4)_{0.3}$ heterojunction implies a faster electron transfer rate and smaller electron–hole recombination effect. In addition, the EIS equivalent circuit can be used to evaluate the charge-transfer abilities of photoelectrochemical systems, where the double-layer capacitance (C_{dl}) is the double layer charge storage capacity at the semiconductor/electrolyte interface and R_{ct} is the charge-transfer resistance at the same interface.[51] To verify the superior photo-generated carrier separation performance of $(BiFeO_3/Ag_{0.05})/(g\text{-}C_3N_4)_{0.3}$, EIS measurements were carried out by varying the potential from 0.15 V to 0.25 V (*versus* saturated calomel electrode (SCE)) in the dark. Fitting to the circuit equivalent, the R_{ct} and C_{dl} parameters of the different photocatalysts were obtained, as displayed in Fig. 7c and d, respectively. The electron lifetime (τ) at the depletion layer of the photocatalysts was calculated according to eqn (1), as follows:[52]

$$\tau = R_{ct}C_{dl} \quad (1)$$

Fig. 7e presents the electron lifetime of g-C_3N_4, $BiFeO_3$, $BiFeO_3/Ag_{0.05}$, and $(BiFeO_3/Ag_{0.05})/(g\text{-}C_3N_4)_{0.3}$, where a shorter lifetime means faster charge transfer ability given that the amount of electrons in the depletion layer of the photocatalysts is very low. The electron lifetime follows the order of g-C_3N_4 > $BiFeO_3$ > $BiFeO_3/Ag_{0.05}$ > $(BiFeO_3/Ag_{0.05})/(g\text{-}C_3N_4)_{0.3}$. The Z-scheme $(BiFeO_3/Ag_{0.05})/(g\text{-}C_3N_4)_{0.3}$ photocatalytic system has superior photogenerated electron–hole pair separation ability, retaining a greater number of photo-generated carriers for producing radicals, which will enhance the photocatalytic efficiency for the degradation of pollutants.

3.2. Evaluation of photocatalytic activity

3.2.1. Efficiency of photocatalytic degradation of MB. The photocatalytic activity of the $(BiFeO_3/Ag_{0.05})/(g\text{-}C_3N_4)_{0.3}$ heterojunction was assessed by the photocatalytic degradation of MB and calculated using eqn (2), as follows:[53]

$$\text{Degradation}\% = 1 - A/A_0 = 1 - C/C_0 \quad (2)$$

where A_0 is the initial absorbance of the MB solution, A is the final absorbance of the MB solution after illumination, C_0 is the initial concentration of MB solution, and C is the final concentration of MB solution after illumination. Before the photocatalytic degradation of MB, adsorption equilibrium occurs for 30 min in the dark reaction, and the maximum

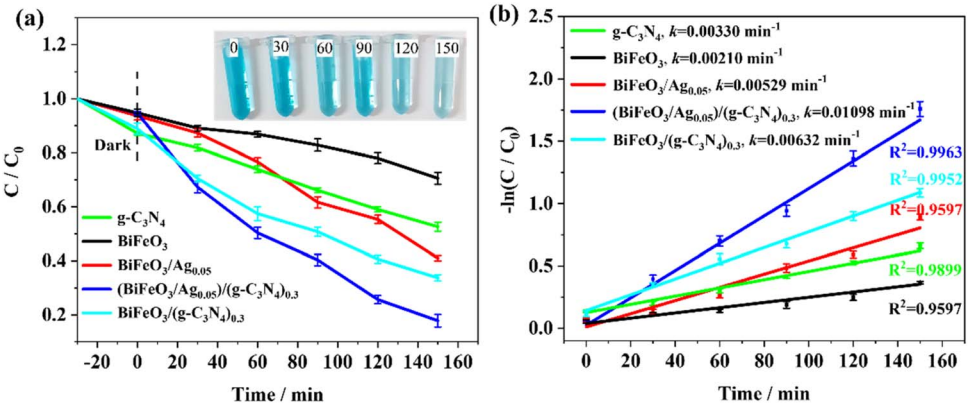

Fig. 8 (a) Catalytic efficiency (inset: the variation of MB solution color by time); (b) catalytic kinetic plots of g-C_3N_4, $BiFeO_3$, $BiFeO_3/Ag_{0.05}$, $(BiFeO_3/Ag_{0.05})/(g\text{-}C_3N_4)_{0.3}$ and $BiFeO_3/(g\text{-}C_3N_4)_{0.3}$ for MB (catalyst = 10 mg, MB = 10 mg L^{-1}, xenon lamp = 300 W).

adsorption of MB reached 13% degradation by g-C_3N_4, while $(BiFeO_3/Ag_{0.05})/(g\text{-}C_3N_4)_{0.3}$ caused 6% degradation, indicating that g-C_3N_4 had stronger dark adsorption ability (Fig. 8a). The corresponding photocatalytic kinetic studies proved that the dark reactions followed a pseudo-second-order kinetic reaction (Fig. S2 and S3). The adsorption kinetic studies were evaluated using eqn (3) and (4), as follows:[54]

$$\ln(q_e - q) = \ln q_e - k_1 t \quad (3)$$

$$t/q = 1/(k_2 q_e^2) + t/q_e \quad (4)$$

where q_e and q are the adsorption capacities at equilibrium and at time t and k_1 and k_2 are rate constants for the pseudo-first-order and pseudo-second-order kinetics, respectively. In the case of g-C_3N_4, the pseudo-second-order kinetic model (R^2 = 0.9948) provides a better fit than the pseudo-first-order kinetic model (R^2 = 0.9002). Similarly, $(BiFeO_3/Ag_{0.05})/(g\text{-}C_3N_4)_{0.3}$ was also significantly better fitted by the pseudo-second-order kinetic model (R^2 = 0.9802) than the pseudo-first-order kinetic model (R^2 = 0.7908). Therefore, both g-C_3N_4 and $(BiFeO_3/Ag_{0.05})/(g\text{-}C_3N_4)_{0.3}$ follow the pseudo-second-order kinetic model during the dark reaction periods. After 40 min of dark adsorption and 150 min illumination, the maximum removal efficiency of MB reached 84.60% by the $(BiFeO_3/Ag_{0.05})/(g\text{-}C_3N_4)_{0.3}$ heterojunction, while that of g-C_3N_4, $BiFeO_3$, $BiFeO_3/Ag_{0.05}$, and $BiFeO_3/(g\text{-}C_3N_4)_{0.3}$ was only 49.2%, 31.3%, 60.0% and 66.3%, respectively. The corresponding UV-vis spectra are shown in Fig. S4, and the MB degradation efficiency was calculated at the maximum absorption wavelength of 664 nm. In addition, the optimum mass ratio of $BiFeO_3$/Ag/g-C_3N_4 in photocatalytic MB degradation was investigated, as shown in Fig. S5. According to Fig. S5a, the $BiFeO_3$/Ag composite achieved the best catalytic effect when the amount of Ag is 5 wt%. Additionally, with a mass fraction of g-C_3N_4 at 30 wt%, the $BiFeO_3$/Ag/g-C_3N_4 composite showed the best catalytic effect (Fig. S5b). The photodegradation rate constant was fitted by the first-order reaction kinetics using eqn (5), as follows:[55]

$$\ln(C/C_0) = -kt \quad (5)$$

where k is the photodegradation rate constant. As shown in Fig. 8b, the rate constant of $(BiFeO_3/Ag_{0.05})/(g\text{-}C_3N_4)_{0.3}$ (k = 0.01163 min^{-1}) is 5.84-times than that of $BiFeO_3$ and 3.26-times than that of g-C_3N_4, demonstrating its superior photocatalytic activity towards MB. The MB removal efficiency of $BiFeO_3$/Ag/g-C_3N_4 is 2.7-times than that of pure $BiFeO_3$ and 1.7-times than that of pure g-C_3N_4, confirming the advantages of the 1D/0D/2D layered architecture and synergistic effect in the $BiFeO_3$/Ag/g-C_3N_4 Z-scheme heterojunction. (i) The 1D/0D/2D multilayered architecture of $BiFeO_3$/Ag/g-C_3N_4 significantly enhanced the specific surface area of single materials, which could provide more accessible surface sites for the adsorption and degradation of MB. (ii) The LSPR enhancement effect of Ag offers the advantages of low cost, improved visible-light absorption and photoelectron transfer.[56] In addition, Ag acts as an electronic bridge, promoting electron transfer between $BiFeO_3$ and g-C_3N_4. (iii) The formation of a Z-scheme heterojunction can retain strong redox potentials by generating holes in the VB of $BiFeO_3$ and electrons in the CB of g-C_3N_4, and simultaneously form $^{\bullet}O_2^-$ and $^{\bullet}OH$ radicals to directly react with pollutants. Table S2 presents a comparison with other semiconductor photocatalysts for the degradation of pollutants. The present $BiFeO_3$/Ag/g-C_3N_4 Z scheme heterojunction displayed an appropriate photo-degradation efficiency, further providing a green and simple method for the construction of visible-light Z-scheme heterojunctions.

3.2.2. Reusability analysis. The photochemical stability and reusability of photocatalysts are key indicators for assessing their catalytic efficiency and long-term performance in practical applications. In this study, the reusability of the $(BiFeO_3/Ag_{0.05})/(g\text{-}C_3N_4)_{0.3}$ heterojunction was evaluated, as shown in Fig. S6. The degradation efficiency of $(BiFeO_3/Ag_{0.05})/(g\text{-}C_3N_4)_{0.3}$ remained 70.3% after four photocatalytic degradation cycling experiments, indicating its satisfactory photocatalytic stability and reusability for the degradation of MB in water.

3.2.3. Photocatalytic mechanism. The bandgap of different photocatalysts can be calculated using the UV-vis DRS and Mott–Schottky methods. Fig. 9a presents the plots of $(\alpha h\nu)^2$ *versus* $h\nu$ for g-C_3N_4, $BiFeO_3$ and $BiFeO_3$/Ag. The bandgap energies of g-C_3N_4, $BiFeO_3$ and $BiFeO_3$/Ag are determined to be 2.79 eV, 2.12 eV, and 1.99 eV, respectively, which are consistent

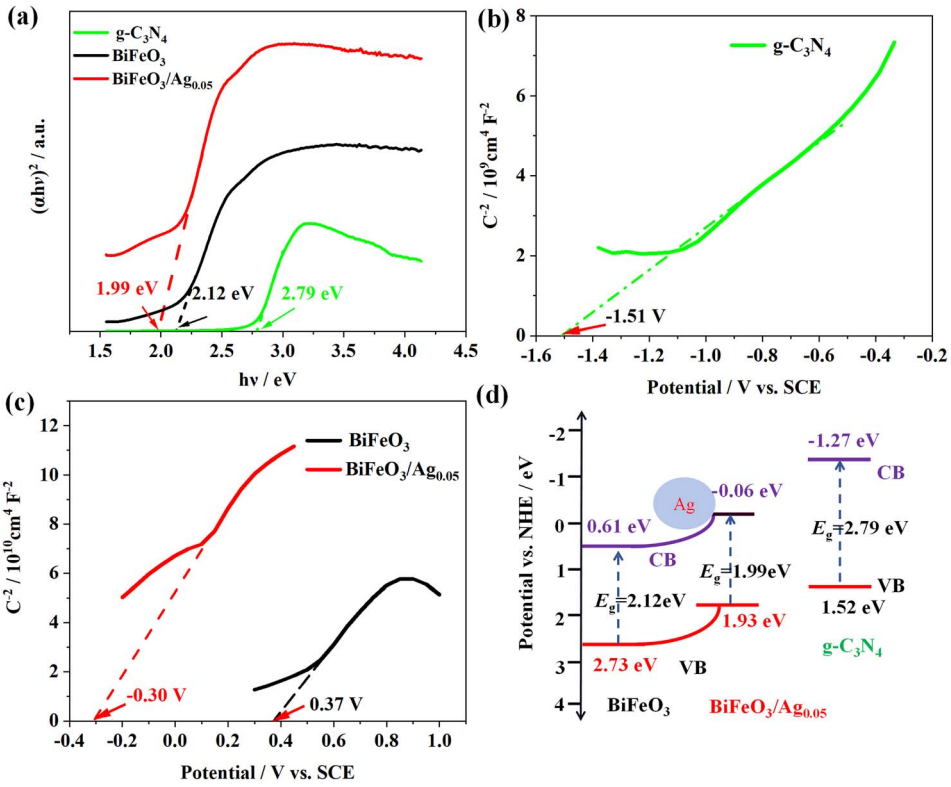

Fig. 9 (a) Plots of $(\alpha h\nu)^2$ *versus* $h\nu$ for g-C_3N_4, $BiFeO_3$ and $BiFeO_3$/Ag. (b and c) Mott–Schottky plots of pure g-C_3N_4 and $BiFeO_3$ and $BiFeO_3$/Ag, respectively. (The Mott–Schottky effect was measured in a 0.5 M Na_2SO_4 solution at 1.0 kHz.) (d) Schematic of the band structures of g-C_3N_4, $BiFeO_3$ and $BiFeO_3$/Ag.

with the literature values.[57] As shown in Fig. 9b and c, the flat-band potentials (V_{fb}) of g-C_3N_4, $BiFeO_3$ and $BiFeO_3$/Ag are −1.51 V, 0.37 V and −0.30 V *versus* SCE, respectively. These flat band potential values are modulated to the normal hydrogen electrode (NHE) values using eqn (6), as follows:[58]

$$V_{fb}(\text{NHE, pH} = 7) = V_{fb}(\text{SCE}) + 0.2415 - 0.059\,(7 - \text{pH of the electrolyte}) \quad (6)$$

It has been reported that the conduction band position (E_{CB}) of n-type semiconductors is very close to V_{fb}; therefore, the E_{CB} values of g-C_3N_4, $BiFeO_3$ and $BiFeO_3$/Ag are −1.27 eV, 0.61 eV and −0.06 eV, respectively.[59] The valence-band edge (E_{VB}) was subsequently calculated using eqn (7), as follows:

$$E_g = E_{VB} - E_{CB} \quad (7)$$

The band structure diagram of the materials is shown in Fig. 9d. The CB and VB potentials of $BiFeO_3$/Ag are more negative than that of $BiFeO_3$, and thus the accumulated photoelectrons on the CB of $BiFeO_3$ easily flow to the Ag nanoparticles. Owing to the lower Fermi level of the Ag nanoparticles, Ag acted as an electron reservoir, surmounting the Schottky barriers at the $BiFeO_3$/Ag interface. The LSPR effect of the Ag nanoparticles induced by the oscillation of their surface electrons could further enhance the visible light harvesting of photocatalysts and promote electron–hole separation.[60,61]

As shown in Fig. 10a, in the photocatalytic systems, *p*-benzoquinone (*p*-BQ), isopropanol (IPA), and methanol (MeOH) were added to the MB solution to capture the superoxide ($^{\bullet}O_2^-$), $^{\bullet}OH$, and h^+, respectively.[62–64] After adding IPA and *p*-BQ, separately, the degradation efficiency of MB was severely suppressed, indicating that $^{\bullet}OH$ and $^{\bullet}O_2^-$ play a major role in the degradation process compared to h^+, respectively. To ensure effective quenching of target free radicals, we investigated the effect of different scavenger concentrations on the photocatalytic degradation of MB (Fig. S7). As the scavenger concentration increased from 10 mM to 30 mM, the free radical scavenging efficiency remained nearly constant, and thus we selected a scavenger concentration of 30 mM for comparison.

Electron paramagnetic resonance (EPR) experiments were conducted for $(BiFeO_3/Ag_{0.05})/(g\text{-}C_3N_4)_{0.3}$ to further verify the production of $^{\bullet}OH$ and $^{\bullet}O_2^-$. As shown in Fig. 10b and c, no EPR signals were detected in the dark. The EPR signals of $^{\bullet}OH$ and $^{\bullet}O_2^-$ can be clearly seen under light irradiation, which is consistent with the results of the active species scavenging experiments. This suggests that $(BiFeO_3/Ag_{0.05})/(g\text{-}C_3N_4)_{0.3}$ can produce $^{\bullet}OH$ and $^{\bullet}O_2^-$ radicals, confirming the hypothesis of constructing a Z-scheme photocatalytic system.

Furthermore, the main intermediates yielded during the photocatalytic degradation of MB and the possible degradation pathways were investigated using liquid chromatography-mass spectrometry (LC-MS). According to the *m*/*z* ratios obtained in positive mode, a total of 15 dominant structures was identified

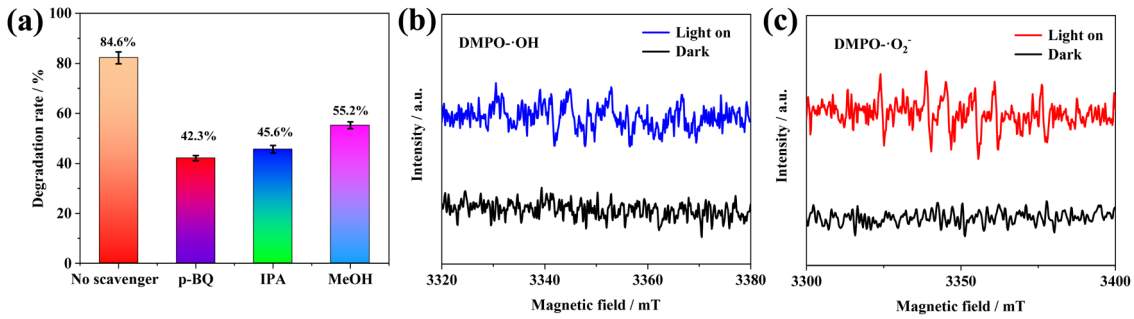

Fig. 10 (a) Effect of scavengers on the photocatalytic removal of MB by $(BiFeO_3/Ag_{0.05})/(g\text{-}C_3N_4)_{0.3}$ (scavengers' content: 30 mM *p*-BQ, 30 mM IPA, and 30 mM MeOH). EPR spectra of $(BiFeO_3/Ag_{0.05})/(g\text{-}C_3N_4)_{0.3}$ for (b) DMPO–$^{\cdot}OH$ and (c) DMPO–$^{\cdot}O_2^-$.

under 0, 30, 90, 150 min light irradiation, as shown in Fig. S8, and the possible three degradation pathways under $^{\cdot}OH$ and $^{\cdot}O_2^-$ induction are shown in Fig. 11. The mass spectrum of MB shows a prominent molecular ion peak at $m/z = 284$, which is consistent with a previous report.[65] The $^{\cdot}OH$ and $^{\cdot}O_2^-$ radicals may further cause the MB degradation pathways to proceed through demethylation, oxidative, and ring opening to the final fragmentation, and eventually mineralization was achieved.[66,67] In pathway I, the original MB is demethylated to form intermediate P2 ($m/z = 270$), followed by the loss of another methyl group to form P3 ($m/z = 256$), and finally converted to the product P4 ($m/z = 198$) through demethylation and deamination. In pathway II, the MB molecule is converted to two oxidative products, P5 ($m/z = 317$) and P8 ($m/z = 273$), by the formation of a sulfoxide group and demethylation process. According to the easily broken bond of N–CH_3, and the C–N or C–S bond on the central heterocycle of MB, the P5 and P8 intermediates can be degraded into small forms by desulfurization, demethylation, hydroxylation reactions.[68] In pathway III, the MB molecule is demethylated to form P12 ($m/z = 228$), subsequently converting to P13 ($m/z = 280$) by the oxidation of the C–S bond on the central heterocycle to sulfoxide, which is further converted to P14 ($m/z = 173$) and P15 ($m/z = 141$) through the cleavage of the central ring. Eventually, the short

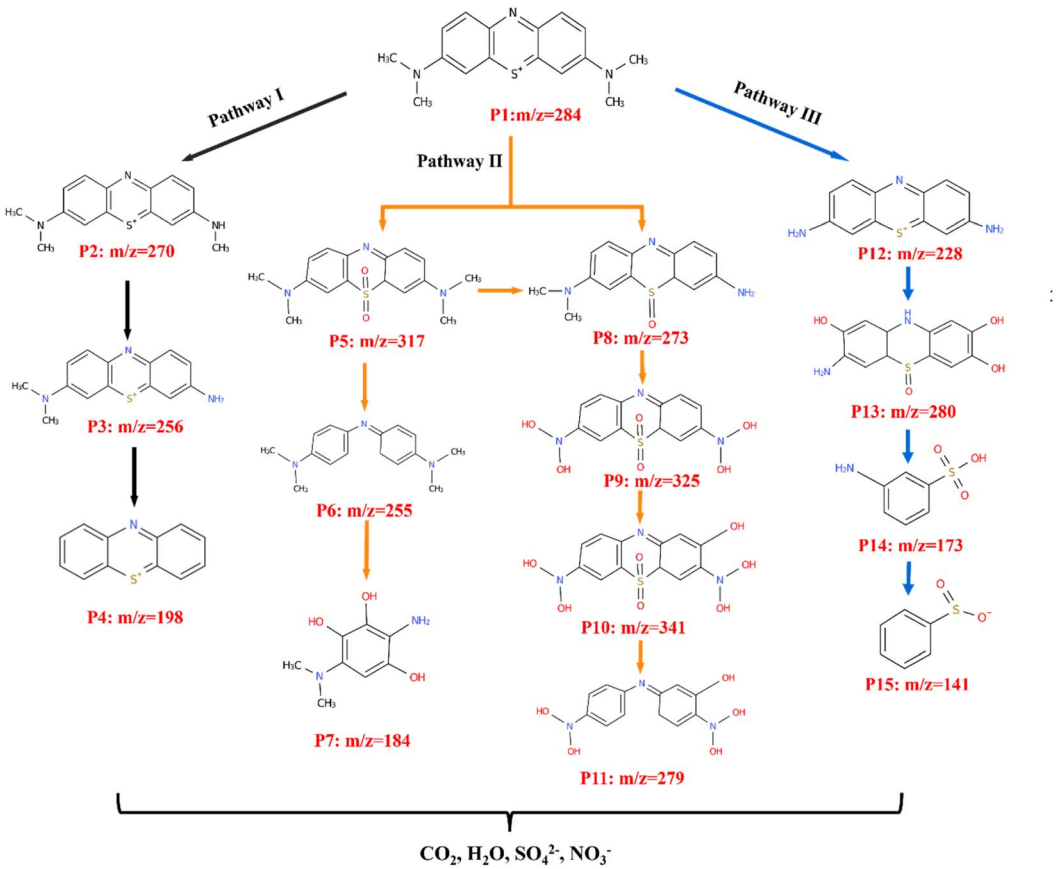

Fig. 11 Possible photocatalytic degradation pathways of MB.

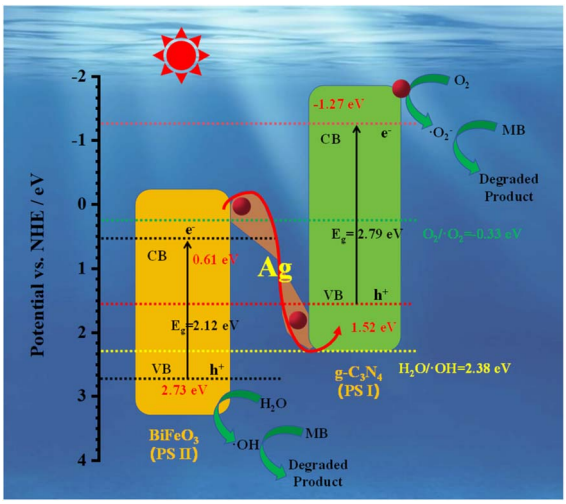

Fig. 12 Possible photocatalytic mechanism of the Z-scheme ($BiFeO_3$/$Ag_{0.05}$)/($g\text{-}C_3N_4$)$_{0.3}$ system.

open ring structures were completely mineralized into CO_2, H_2O, SO_4^{2-}, NO_3^- and some inorganic compounds.[69]

Considering the radical scavenging experiments and the bandgap configuration of the prepared $g\text{-}C_3N_4$ and $BiFeO_3$, a possible photocatalytic mechanism is proposed, as shown in Fig. 12. $g\text{-}C_3N_4$ is unable to produce $^{\bullet}OH$ (its E_{VB} is more negative than 2.38 eV), while $BiFeO_3$ is unable to produce $^{\bullet}O_2^-$ (its E_{CB} is more positive than −0.33 eV). The Z-scheme heterojunction of $BiFeO_3$/Ag/$g\text{-}C_3N_4$ is formed to achieve the photocatalytic degradation of MB. Given that the E_{CB} of $g\text{-}C_3N_4$ (−1.27 eV) is more negative than that of $O_2/^{\bullet}O_2^-$ (−0.33 eV *vs.* NHE), it can capture adsorbed oxygen to form $^{\bullet}O_2^-$ radicals. The E_{VB} of $BiFeO_3$ (−2.73 eV) is more positive than the reduction potential of $H_2O/^{\bullet}OH$ (2.38 eV *vs.* NHE), and $^{\bullet}OH$ radicals are created.[70] The photogenerated electrons from the CB of $BiFeO_3$ can rapidly transfer to $g\text{-}C_3N_4$ through plasmonic Ag, and combine with the holes from the VB of $g\text{-}C_3N_4$. Consequently, the electrons from the CB of $g\text{-}C_3N_4$ and the holes from the VB of $BiFeO_3$ are effectively separated. The MB in solution is oxidized and degraded in the presence of $^{\bullet}OH$ and $^{\bullet}O_2^-$ to CO_2, H_2O, mineral acids.[71] The possible reactions are as follows:

$$BiFeO_3/Ag/g\text{-}C_3N_4 + h\nu \rightarrow h^+ + e^- + BiFeO_3/Ag/g\text{-}C_3N_4^* \quad (8)$$

$$H_2O + h^+ \rightarrow {}^{\bullet}OH + H^+ \quad (9)$$

$$O_2 + e^- \rightarrow {}^{\bullet}O_2^- \quad (10)$$

$$^{\bullet}OH + MB \rightarrow \text{degraded product} \quad (11)$$

$$^{\bullet}O_2^- + MB \rightarrow \text{degraded product} \quad (12)$$

4. Conclusion

In summary, a Z-scheme heterojunction of 1D/0D/2D $BiFeO_3$/Ag/$g\text{-}C_3N_4$ was constructed to enhance the photocatalytic activity in degradation of organic dyes under visible light irradiation. The structural parameters, optical properties, photocatalytic dye degradation, and dielectric properties of the materials were assessed by XRD, XPS, BET, SEM, EDX, UV-vis DRS, PL, electrochemical and photocatalytic degradation testing. The EPR and free radical scavenging experiments confirmed the active species ($^{\bullet}OH$ and $^{\bullet}O_2^-$) for the decomposition of MB, demonstrating the possible photocatalytic mechanism. This study provides a feasible way for improving the visible light degradation of dyes in wastewater, and has significant reference for the design and synthesis of novel Z-scheme heterojunction photocatalysts with multidimensional contact interfaces.

Author contributions

Donghai Li: investigation, writing – original draft, data curation and validation; Yunrui Xu: visualization, investigation; Shilin Zhang: visualization, investigation; Linping Wang: writing – review & editing, writing – original draft, supervision, investigation, funding acquisition.

Conflicts of interest

We declare that there is no conflict of interest to this work.

Data availability

The data supporting this article have been included as part of the SI. No additional datasets were generated or analyzed during this study.

Supplementary information: The authors declare that the data supporting the findings of this study are available within the paper and its SI. Isotherm linear plots, dark reaction kinetic curves, effects of Ag and $g\text{-}C_3N_4$ mass fractions on efficiency, LC-MS spectra, photocatalytic stability and comparison table of photocatalytic degradation. See DOI: **https://doi.org/10.1039/d5ra04825g**.

Acknowledgements

This work was funded by the Natural Science Foundation of Qinghai Province (no. 2021-ZJ-964Q) and the Youth Research Fund Project of Qinghai University (no. 2020-QGY-8).

References

1 F. Deng, J. Peng, X. Li, X. Luo, P. Ganguly, S. C. Pillai, B. Ren, L. Ding and D. D. Dionysiou, Metal sulfide-based Z-scheme heterojunctions in photocatalytic removal of contaminants, H_2 evolution and CO_2 reduction: Current status and future perspectives, *J. Cleaner Prod.*, 2023, **416**, 137957–137976.
2 K. Parida, N. Baliarsingh, B. S. Patra and J. Das, Copperphthalocyanine immobilized Zn/Al LDH as photocatalyst under solar radiation for decolorization of methylene blue, *J. Mol. Catal. A: Chem.*, 2007, **267**, 202–208.
3 A. C. Pradhan and K. Parida, Facile synthesis of mesoporous composite Fe/Al_2O_3–MCM-41: an efficient adsorbent/catalyst

for swift removal of methylene blue and mixed dyes, *J. Mater. Chem.*, 2012, **22**, 7567–7579.
4 P. Mohapatra and K. Parida, Photocatalytic activity of sulfate modified titania 3: Decolorization of methylene blue in aqueous solution, *J. Mol. Catal. A: Chem.*, 2006, **258**, 118–123.
5 S. Nayak, K. K. Das and K. Parida, Indulgent of the physiochemical features of MgCr-LDH nanosheets towards photodegradation process of methylene blue, *J. Colloid Interface Sci.*, 2023, **634**, 121–137.
6 S. Y. Kim, I. Y. Kim, S.-H. Park, M. Hwangbo and S. Hwangbo, Novel ultrasonic technology for advanced oxidation processes of water treatment, *RSC Adv.*, 2024, **14**, 11939–11948.
7 S. M. H. Al-Jawad, K. H. Aboud, N. J. Imran and S. Y. Taher, Copper doping of CdS nanoflakes and nanoflowers for efficient photocatalytic degradation of MB and MV dyes, *Plasmonics*, 2025, **20**, 983–1002.
8 C. Zhao, X. Li, L. Yue, S. Yuan, X. Ren, Z. Zeng, X. Hu, Y. Wu and Y. He, One-step preparation of novel Bi-Bi_2O_3/$CdWO_4$ Z-scheme heterojunctions with enhanced performance in photocatalytic NH_3 synthesis, *J. Alloys Compd.*, 2023, **968**, 171956–171969.
9 M. A. Gatou, A. Syrrakou, N. Lagopati and E. A. Pavlatou, Photocatalytic TiO_2-based nanostructures as a promising material for diverse environmental applications: a review, *Reactions*, 2024, **5**, 135–194.
10 M. Alhaddad and M. S. Amin, Removal of ciprofloxacin applying Pt@$BiVO_4$-g-C_3N_4 nanocomposite under visible light, *Opt. Mater.*, 2022, **124**, 111976–111986.
11 B. Malathi, Y. Mori, S. Harish and A. Nakamura, Investigation of 2D-layered photocatalytic semiconductors with enhanced heterojunction region for photocatalytic degradation, *J. Mater. Sci.: Mater. Electron.*, 2024, **35**, 1236–1250.
12 X. Li, Y. Huang, W. Ho, S. Han, P. Wang, S. Lee and Z. Zhang, Modulation of sulfur vacancies at $ZnIn_2S_4$-δ/g-C_3N_4 heterojunction interface for successive C-H secession in photocatalytic gaseous formaldehyde complete oxidation, *Appl. Catal., B*, 2023, **338**, 123048–123060.
13 M. Atighi, G. Falahati, M. Hasanzadeh, N. Gholami, H. Ahmadi and M. Najafi, Fabrication of a graphene oxide/zeolitic imidazolate framework-8 (GO/ZIF-8) composite for enhanced adsorptive and piezo-assisted photocatalytic removal of organic dyes, *New J. Chem.*, 2025, **49**, 10751–10765.
14 Y. Xu, Y. Liang, Q. He, R. Xu, D. Chen, X. Xu and H. Hu, Review of doping $SrTiO_3$ for photocatalytic applications, *Bull. Mater. Sci.*, 2022, **46**, 6.
15 N. A. Neto, A. Lima, R. Wilson, T. Nicacio, M. Bomio and F. Motta, Heterostructures obtained by ultrasonic methods for photocatalytic application: A review, *Mater. Sci. Semicond. Process.*, 2022, **139**, 106311–106321.
16 C. Nie, X. Wang, P. Lu, Y. Zhu, X. Li and H. Tang, Advancements in S-scheme heterojunction materials for photocatalytic environmental remediation, *J. Mater. Sci. Technol.*, 2024, **169**, 182–198.
17 L. Zheng, Y. Wei, C. Wang, H. Liu, L. Li, M. Huang, Y. Huang, L. Fan and J. Wu, Construction of direct WO_3/g-C_3N_4 Z-scheme heterojunction for degrading flotation agent effectively, *Ceram. Int.*, 2024, **50**, 38860–38870.
18 S. D. Lakshmi and I. B. S. Banu, Multiferroism and magnetoelectric coupling in single-phase Yb and X (X = Nb, Mn, Mo) co-doped $BiFeO_3$ ceramics, *J. Sol-Gel Sci. Technol.*, 2019, **89**, 713–721.
19 S. Mansingh, S. Sultana, R. Acharya, M. K. Ghosh and K. M. Parida, Efficient photon conversion via double charge dynamics CeO_2–$BiFeO_3$ p–n heterojunction photocatalyst promising toward N_2 fixation and phenol–Cr(VI) detoxification, *Inorg. Chem.*, 2020, **59**, 3856–3873.
20 C. Li, Z. Li, S. Guo, X. Li, Q. Cheng and S. Meng, Sensitivity enhancement by employing $BiFeO_3$ and graphene hybrid structure in surface plasmon resonance biosensors, *Opt. Mater.*, 2021, **121**, 111618–111627.
21 Y. Nassereddine, M. Benyoussef, B. Asbani, M. El Marssi and M. Jouiad, Recent advances toward enhanced photocatalytic proprieties of $BiFeO_3$-based materials, *Nanomaterials*, 2024, **14**, 51–81.
22 I. Shakir, Synthesis of Gd doped $BiFeO_3$/g-C_3N_4 composite: Enhancement of solar mediated photocatalytic performance, *Mater. Sci. Eng., B*, 2024, **302**, 117252–117263.
23 M. P. McOyi, K. T. Mpofu, M. Sekhwama and P. Mthunzi-Kufa, Developments in localized surface plasmon resonance, *Plasmonics*, 2024, **20**, 5481–5520.
24 S. Ni, Z. Fu, L. Li, M. Ma and Y. Liu, Step-scheme heterojunction g-C_3N_4/TiO_2 for efficient photocatalytic degradation of tetracycline hydrochloride under UV light, *Colloids Surf., A*, 2022, **649**, 129475–129487.
25 J. Tang, R. Wang, M. Liu, Z. Zhang, Y. Song, S. Xue, Z. Zhao and D. D. Dionysiou, Construction of novel Z-scheme Ag/$FeTiO_3$/Ag/$BiFeO_3$ photocatalyst with enhanced visible-light-driven photocatalytic performance for degradation of norfloxacin, *Chem. Eng. J.*, 2018, **351**, 1056–1066.
26 Z. H. Jabbar, B. H. Graimed, M. A. Issa, S. H. Ammar, S. E. Ebrahim, H. J. Khadim and A. A. Okab, Photocatalytic degradation of Congo red dye using magnetic silica-coated Ag_2WO_4/Ag_2S as Type I heterojunction photocatalyst: Stability and mechanisms studies, *Mater. Sci. Semicond. Process.*, 2023, **153**, 107151–107166.
27 V. Kashyap, H. Pawar, I. Sihmar, C. Kumar, A. Kumar, S. Kumar, N. Chaudhary, N. Goyal and K. Saxena, X-ray analysis of Ag nanoparticles on Si wafer and influence of Ag nanoparticles on Si nanowire-based gas sensor, *Appl. Phys. A*, 2024, **130**, 238–251.
28 Y. Guo, L. Zhu, J. Wang and J. Li, Comprehensive computational investigation of structural and mechanical characteristics of crystalline C_3N_4 under high pressure based on experimental data, *Phys. B*, 2024, **674**, 415604–415611.
29 D. A. Rusakov, A. M. Abakumov, K. Yamaura, A. A. Belik, G. Van Tendeloo and E. Takayama-Muromachi, Structural evolution of the $BiFeO_3$–$LaFeO_3$ system, *Chem. Mater.*, 2011, **23**, 285–292.

30 M. Ghosh, S. Mandal, A. Roy, S. Chakrabarty, G. Chakrabarti and S. K. Pradhan, Enhanced antifungal activity of fluconazole conjugated with Cu-Ag-ZnO nanocomposite, *Mater. Sci. Eng., C*, 2020, **106**, 110160–110170.

31 Q. Xiang, J. Yu and M. Jaroniec, Preparation and enhanced visible-light photocatalytic H_2-production activity of graphene/C_3N_4 composites, *J. Phys. Chem. C*, 2011, **115**, 7355–7363.

32 F. Dong, Z. Wang, Y. Sun, W.-K. Ho and H. Zhang, Engineering the nanoarchitecture and texture of polymeric carbon nitride semiconductor for enhanced visible light photocatalytic activity, *J. Colloid Interface Sci.*, 2013, **401**, 70–79.

33 J. Liu, T. Zhang, Z. Wang, G. Dawson and W. Chen, Simple pyrolysis of urea into graphitic carbon nitride with recyclable adsorption and photocatalytic activity, *J. Mater. Chem.*, 2011, **21**, 14398–14401.

34 H. Yan and H. Yang, TiO_2–g-C_3N_4 composite materials for photocatalytic H_2 evolution under visible light irradiation, *J. Alloys Compd.*, 2011, **509**, L26–L29.

35 S. J. J. Kay, N. Chidhambaram, A. Thirumurugan, S. Shanavas, P. Sakthivel and R. S. Rimal Isaac, Stoichiometric balancing of bismuth ferrite-perovskite nanoparticles: comparative investigations on biogenic versus conventional chemical synthesis, *J. Mater. Sci.: Mater. Electron.*, 2023, **34**, 2034–2048.

36 M. B. Islam, M. J. Haque, N. M. Shehab and M. S. Rahman, Synthesis and characterization (optical and antibacterial) of silver doped zinc oxide nanoparticles, *Open Ceram.*, 2023, **14**, 100370–100376.

37 Z. Du, Y. Li, D. Kuang, W. Wang, F. Yang, J. Yang and L. Hou, Insight into the synergistic effect of adsorption and photocatalysis for the removal of organic dye pollutants by novel $BiFeO_3$@GO fibers, *J. Mater. Sci.: Mater. Electron.*, 2023, **34**, 589–607.

38 D. A. Upar, D. Gogoi, M. R. Das, B. Naik and N. N. Ghosh, Facile synthesis of g-C_3N_4-exfoliated $BiFeO_3$ nanocomposite: a versatile and efficient S-scheme photocatalyst for the degradation of various textile dyes and antibiotics in water, *ACS Omega*, 2023, **8**, 38524–38538.

39 S. Sharma and M. Kumar, Structural and magnetic properties and graphene-induced photocatalytic activity of $BiFeO_3$ ceramics, *J. Supercond. Novel Magn.*, 2023, **36**, 1193–1202.

40 K. Saravanakumar and C. M. Park, Rational design of a novel $LaFeO_3$/g-C_3N_4/$BiFeO_3$ double Z-scheme structure: Photocatalytic performance for antibiotic degradation and mechanistic insight, *Chem. Eng. J.*, 2021, **423**, 130076–130088.

41 Q. Huang, J. Yu, S. Cao, C. Cui and B. Cheng, Efficient photocatalytic reduction of CO_2 by amine-functionalized g-C_3N_4, *Appl. Surf. Sci.*, 2015, **358**, 350–355.

42 J. Zhang, Y. Zheng, H. Zheng, T. Jing, Y. Zhao and J. Tian, Porous oxygen-doped g-C_3N_4 with the different precursors for excellent photocatalytic activities under visible light, *Materials*, 2022, **15**, 1391–1405.

43 D. Gao, Q. Xu, J. Zhang, Z. Yang, M. Si, Z. Yan and D. Xue, Defect-related ferromagnetism in ultrathin metal-free g-C_3N_4 nanosheets, *Nanoscale*, 2014, **6**, 2577–2581.

44 A. Joseph, R. Jayakrishnan, A. M. Anand and V. Thomas, Ag-doped BiOBr nanoparticles: a grander photocatalyst, *J. Mater. Sci.: Mater. Electron.*, 2025, **36**, 637–657.

45 P. Duan, Q. Xu, S. Shen, Y. Zhang, L. Zhang, F. Fu and X. Liu, One-pot modification on cotton fabric using an emulsion of Ag NPs protected by mercaptosuccinic acid to achieve durably antibacterial effect, *Fibers Polym.*, 2019, **20**, 1803–1811.

46 S. Nayak and K. Parida, Dynamics of charge-transfer behavior in a plasmon-induced quasi-type-II p–n/n–n dual heterojunction in Ag@Ag_3PO_4/g-C_3N_4/NiFe LDH nanocomposites for photocatalytic Cr(VI) reduction and phenol oxidation, *ACS Omega*, 2018, **3**, 7324–7343.

47 J. Xu, T. Qin, W. Chen, J. Lv, X. Zeng, J. Sun, Y.-y. Li and J. Zhou, Synergizing piezoelectric and plasmonic modulation of Ag/$BiFeO_3$ fibrous heterostructure toward boosted photoelectrochemical energy conversion, *Nano Energy*, 2021, **89**, 106317–106326.

48 W. Su, S. S. Wei, S. Q. Hu and J. X. Tang, Preparation of TiO_2/Ag colloids with ultraviolet resistance and antibacterial property using short chain polyethylene glycol, *J. Hazard. Mater.*, 2009, **172**, 716–720.

49 K.-C. Lee, S.-J. Lin, C.-H. Lin, C.-S. Tsai and Y.-J. Lu, Size effect of Ag nanoparticles on surface plasmon resonance, *Surf. Coat. Technol.*, 2008, **202**, 5339–5342.

50 L. Wang, Y. Meng, Y. Zhang, C. Zhang, Q. Xie and S. Yao, Photoelectrochemical aptasensing of thrombin based on multilayered gold nanoparticle/graphene-TiO_2 and enzyme functionalized graphene oxide nanocomposites, *Electrochim. Acta*, 2017, **249**, 243–252.

51 J. Ângelo, P. Magalhães, L. Andrade and A. Mendes, Characterization of TiO_2-based semiconductors for photocatalysis by electrochemical impedance spectroscopy, *Appl. Surf. Sci.*, 2016, **387**, 183–189.

52 L. Andrade, S. M. Zakeeruddin, M. K. Nazeeruddin, H. A. Ribeiro, A. Mendes and M. Grätzel, Influence of sodium cations of N_3 dye on the photovoltaic performance and stability of dye-sensitized solar cells, *ChemPhysChem*, 2009, **10**, 1117–1124.

53 Y. Zhang, Y. Wang, J. Li, J. Xie, W. Wang and Z. Fu, Enhanced photocatalytic activity of Z-scheme meso-$BiVO_4$-Au-CdS for degradation of Rhodamine B, *J. Wuhan Univ. Technol., Mater. Sci. Ed.*, 2024, **39**, 869–876.

54 A. K. Sasmal, J. Pal, R. Sahoo, P. Kartikeya, S. Dutta and T. Pal, Superb dye adsorption and dye-sensitized change in Cu_2O–Ag crystal faces in the dark, *J. Phys. Chem. C*, 2016, **120**, 21580–21588.

55 Z. Long, X. Zheng and H. Shi, Construction of $BiVO_4$/CoPc S-scheme heterojunctions with enhanced photothermal-assisted photocatalytic activity, *Sci. China Mater.*, 2024, **67**, 550–561.

56 S. Patnaik, G. Swain and K. M. Parida, Highly efficient charge transfer through a double Z-scheme mechanism by a Cu-promoted MoO_3/g-C_3N_4 hybrid nanocomposite with

superior electrochemical and photocatalytic performance, *Nanoscale*, 2018, **10**, 5950–5964.

57 X. Zhou, L. Peng, L. Xu, J. Luo, X. Ning, X. Zhou, F. Peng and X. Zhou, Pd(II), Pt(II) metallosupramolecular complexes as Single-Site Co-Catalyst for photocatalytic H_2 evolution, *Chem. Eng. J.*, 2023, **474**, 145967–145978.

58 A. Balakrishnan, E. S. Kunnel, R. Sasidharan, M. Chinthala and A. Kumar, Tailored citric acid-functionalized carbon nitride homojunction-immobilized carboxymethyl cellulose 3D photocatalytic hydrogels: A multifaceted approach toward environmental remediation, *ACS Sustainable Chem. Eng.*, 2024, **12**, 5169–5185.

59 L. Su, N. Qin, W. Xie, J. Fu and D. Bao, The surface-plasmon-resonance and band bending effects on the photoluminescence enhancement of Ag-decorated ZnO nanorods, *J. Appl. Phys.*, 2014, **116**, 063108–063116.

60 L. Panda, A. Pradhan, E. Subudhi, R. K. Sahoo and B. Nanda, Ag-loaded $BiFeO_3$/CuS heterostructured based composite: an efficient photocatalyst for removal of antibiotics and antibacterial activities, *Environ. Sci. Pollut. Res.*, 2024, **31**, 5540–5554.

61 Y. K. Lee, C. H. Jung, J. Park, H. Seo, G. A. Somorjai and J. Y. Park, Surface plasmon-driven hot electron flow probed with metal-semiconductor nanodiodes, *Nano Lett.*, 2011, **11**, 4251–4255.

62 H. Xing, J. Shi, Y. Li and J. Wu, Visible light driven generation of dual active oxygen species on Zr-MOF/g-C_3N_4 photocatalyst for highly selective photocatalytic oxidation of sulfides to sulfoxides, *Inorg. Chem. Commun.*, 2024, **162**, 112129–112136.

63 K. Peng, Z. Fan, Y. Wang, Y. Xie and Y. Ling, Construction of TiO_2/$SnIn_4S_8$ heterojunction to promotion photogenerated carrier separation and enhance photocatalytic hydrogen production via superoxide radical active species, *Int. J. Hydrogen Energy*, 2024, **60**, 835–844.

64 S. Asgari, G. Mohammadi Ziarani, A. Badiei and Y. Vasseghian, Zr-UiO-66, ionic liquid ($HMIM^+TFSI^-$), and electrospun nanofibers (polyacrylonitrile): All in one as a piezo-photocatalyst for degradation of organic dye, *Chem. Eng. J.*, 2024, **487**, 150600–150611.

65 Y. Zhong, X. Wan, X. Lian, W. Cheng, X. Ma and D. Wang, Hydroxylamine facilitated catalytic degradation of methylene blue in a Fenton-like system for heat-treatment modified drinking water treatment residues, *Environ. Sci. Pollut. Res.*, 2023, **30**, 79282–79296.

66 M. V. Nikolic, Z. Z. Vasiljevic, M. Dimitrijevic, N. Radmilovic, J. Vujancevic, M. Tanovic and N. B. Tadic, Natural sunlight driven photocatalytic degradation of methylene blue and Rhodamine B over nanocrystalline Zn_2SnO_4/SnO_2, *Nanomaterials*, 2025, **15**, 1138–1163.

67 W. Ahmad, N. Ahmad, S. Rasheed, M. I. Nabeel, A. Mohyuddin, M. T. Riaz and D. Hussain, Silica-based superhydrophobic and superoleophilic cotton fabric with enhanced self-cleaning properties for oil–water separation and methylene blue degradation, *Langmuir*, 2024, **40**, 5639–5650.

68 Y. Cai, C. Qiu, K. Yang, B. Tian and Y. Bi, Adsorption–degradation of methylene blue by natural manganese ore: kinetics, characterization, and mechanism, *Int. J. Environ. Sci. Technol.*, 2024, **21**, 1817–1830.

69 A. Garg, A. Chauhan, C. Agnihotri, B. P. Singh, V. Mondem, S. Basu and S. Agnihotri, Sunlight active cellulose/g-C_3N_4/TiO_2 nano-photocatalyst for simultaneous degradation of methylene blue dye and atenolol drug in real wastewater, *Nanotechnology*, 2023, **34**, 505705–505719.

70 Q. Xia, X. Liu, H. Li, Y. Guan, J. Chen, Y. Chen, Z. Hu and W. Gao, Construction of the Z-scheme Cu_2O-Ag/AgBr heterostructures to enhance the visible-light-driven photocatalytic water disinfection and antibacterial performance, *J. Alloys Compd.*, 2024, **980**, 173665–173676.

71 K. Parvathalu, K. Rajitha, B. Chandrashekar, K. Sathvik, K. Pranay Bhasker, B. Sreenivas, M. Pritam, P. Pushpalatha, K. Moses and P. Bala Bhaskar, Biomimetic synthesis of copper nanoparticles using Tinospora cordifolia plant Leaf extract for photocatalytic activity applications, *Plasmonics*, 2024, **19**, 825–834.